

Supplemental Information to “Spatial variations in the composition of turbidites due to hydrodynamic fractionation”

David R. Pyles^{1*}, Kyle M. Straub², Jane G. Stammer¹

¹Chevron Center of Research Excellence, Department of Geology and Geological Engineering, Colorado School of Mines, Golden, Colorado, USA

²Department of Earth and Environmental Sciences, Tulane University, New Orleans, Louisiana, USA

Corresponding author: D.R. Pyles, Chevron Center of Research Excellence, Department of Geology and Geological Engineering, Colorado School of Mines, Golden, Colorado, USA.
(dpyles@mines.edu)

1. Experimental Design

The two experiments were conducted in a 6-m long, 4-m wide, and 2.2-m deep basin equipped with an XYZ data collection carriage that houses an acoustic Doppler profiler (ADP) and a 35-MHz ultrasonic topography scanning system (Supplemental Figure 1). The experiments were conducted on a false floor with a 10% slope in the primary flow direction. The basin is surrounded by a moat and perimeter drain that removed the currents when they reached the edge of the false floor serving to extinguish reflections of the currents back onto the floor. The false floor is lined with a 15:1 mixture of sand and cement mortar that was strong enough to prevent erosion by the experimental flows. The experimental turbidity currents were composed of tap water, dissolved CaCl₂ salt, and suspended sediment. The currents had 4% excess density relative to the tap water in the basin: 50% of the excess density was due to suspended sediment and 50% was from the dissolved salt. Each experiment consisted of five turbidity currents; each had approximately the same input values for current height, fluid discharge, duration, and excess density, allowing us to isolate the influence of grain density and shape on current behavior and spatial changes in composition. The first experiment tested how grain density influences the spatial distribution of particles, termed the density experiment; whereas the second experiment tested how grain shape influences the spatial distribution of particles, termed the shape experiment. In the density experiment, 50% by volume of the sediment was spherical soda-lime glass ($\rho_s = 2.5 \text{ g/cm}^3$) and 50% was spherical zirconia-silicate glass ($\rho_s = 3.85 \text{ g/cm}^3$). The D5, D50, and D95 of the cumulative size distribution of the spherical soda-lime glass had nominal diameters of 85 μm , 112 μm , and 167 μm , respectively (Supplemental

Figure 2a). The D5, D50, and D95 of the cumulative grain-size distribution of the spherical zirconia-silicate glass had nominal diameters of 64 μm , 101 μm , and 148 μm , respectively. In the shape experiment, 50% by volume of the sediment was spherical soda-lime glass ($\rho_s = 2.5 \text{ g/cm}^3$) and 50% was angular soda-lime glass ($\rho_s = 2.5 \text{ g/cm}^3$). The D5, D50, and D95 of the cumulative size distribution of the spherical soda-lime glass had nominal diameters of 85 μm , 112 μm , and 167 μm , respectively. The D5, D50, and D95 of the cumulative size distribution of the angular soda-lime glass had nominal diameters of 90 μm , 141 μm , and 272 μm , respectively (Supplemental Figure 2A). Input cumulative distributions of sediment fall velocity, w_s , were calculated using input cumulative sediment size distributions (Supplemental Figure 2B). Conversion from sediment size to w_s was performed using equation 4 from *Ferguson and Church* [2004].

$$w_s = \frac{RgD^2}{C_1\nu + (0.75C_2RgD^3)^{0.5}} \quad (1)$$

where R is the submerged specific gravity of sediment:

$$R = \frac{(\rho_s - \rho_a)}{\rho_a} \quad (2)$$

ρ_s is sediment density, ρ_a is the ambient fluid density, g is gravitational acceleration, D is particle diameter, and C_1 and C_2 are constants. For spheres (spherical soda-lime glass and spherical zirconia-silicate glass), C_1 and C_2 have known exact values of 18 and 0.4, respectively; whereas, for natural sediment (angular soda-lime glass) C_1 and C_2 have values of approximately 20 and 1.1, respectively [*Ferguson and Church*, 2004]. Dissolved salt was used to simulate the finest portion of suspended sediment within natural turbidity currents, a fraction that is transported to the distal end of a system without loss via deposition. The sediment-saltwater mixture was introduced to the basin via a constant head tank that promotes steady input discharge throughout each individual experimental flow. Currents entered the basin through a momentum extraction box. This box was 0.5 m wide and 0.75 m long in plan view and contained several vertical screens of 5 mm wire mesh which currents passed through prior to entering the experimental basin (Supplemental Figure 1). The momentum extraction box ensured that each flow acted as a sediment-laden plume driven by buoyancy alone. Current thickness and discharge were approximately constant for all flow events at values of 0.11 m and $3 \times 10^{-3} \text{ m}^3/\text{s}$. The duration of each current was 255 ± 47 seconds.

Velocity profiles were collected using a Nortek Aquadopp HR Profiler, which is a pulse-Coherent Acoustic-Doppler Profiler (PCADP). The PCADP measured velocity with a frequency of

1 Hz in roughly cylindrical sampling volumes that were 8×10^{-3} m deep and had a horizontal foot print that varied in diameter from 0.90-to-0.93 m with increasing distance from the transducer. Velocity profiles were collected at many locations within the basin, but here we focus on profiles collected with increasing down-slope distances from the entrance box (increasing in x-direction) centered over the cross-slope midpoint (constant y-position of 2000 mm from left basin side wall). Profiles of current velocity are shown in Supplemental Figure 3 at distances from the proximal basin wall of 0.9, 1.2, 1.5, 1.8 m. Little change in the structure or thickness of the currents with increasing distance from the basin entrance is noted.

The bulk Richardson number:

$$Ri_B = \frac{gh(\rho_c - \rho_a)}{\bar{u}^2} \quad (3)$$

Characterizes how ambient fluid is incorporated into a turbidity current, where \bar{u} is the mean current velocity and h is thickness of the flow. When Ri_B is $\gg 0.25$, velocity shear is insufficient to overcome the tendency for a stratified flow to remain stratified [Turner, 1973]. Ri_B for the experimental currents was 6.7. The relatively high Ri_B and minimal change in current thickness and velocity with distance from the entrance box support minimal entrainment of ambient fluid into the experimental currents during their traverse across the experimental basin.

A 35 MHz ultrasonic transducer connected to a pulse/receiver box was used to make maps of topography before and after each experiment using 588,800 points using a 5 mm (cross stream) and 10 mm (downstream) grid. The precision at each location is better than 0.2 mm. Thickness maps of the deposits of each experiment were constructed by calculating the difference in basin topography before and after the experiments (Supplemental Figure 4).

Aerial photographs of the experimental currents were collected from cameras positioned above the basin. Photographs were collected every 0.25 s. The photographs imaged the passage of the head of the current across the basin. The structure of the flow field associated with the body of each current was imaged by releasing a 0.5 L pulse of red dye at the entrance of the basin about two minutes following the start of each flow (Supplemental Figure 4). These images were used to define the magnitude and direction of the local maximum horizontal velocity throughout the basin.

Following the final current of each experiment the basin was drained and samples of the deposits were manually collected using a cross-shaped grid (Supplemental Figure 4).

2. Analysis of Samples

Samples were split into representative 1-g aliquots using a micro-rotary riffler. Graphite particles having the same grain-size distribution as the sediment were added to each sample in a 2:1 ratio. Graphite serves to separate the individual grains and also increases sample randomization. The sediment and graphite mixture is mounted into 30-mm cups and vigorously mixed with a viscous epoxy resin to prevent density settling. Once hardened, the samples were ground and polished to a 1- μm finish.

Samples were analyzed with QEMSCAN, a quantitative and automated scanning-electron microscope (SEM) system. The QEMSCAN system combines a fully automated FEI Quanta 650 SEM platform with two Bruker silicon-drift energy dispersive X-ray spectrometers (EDS), a four-quadrant solid-state backscatter electron (BSE) detector, and a secondary electron detector. Standard operating conditions are set at an accelerating voltage of 20 kV, a specimen current of 10 nA, and a working distance of ~ 13 mm. The beam diameter is generally between 0.25 – 0.5 μm , however the excitation volume can be up to 5 μm depending on the material analyzed.

Once the beam hits the sample, secondary and backscatter electrons (BSE), and X-rays are emitted and collected by their respective detectors. In this study, we only collected BSE, which are higher-energy electrons reflected from the sample. The intensity of the BSE signal directly relates to the density of the material, which is directly controlled by the atomic number of the elements in the material. Accordingly, for the density experiment, due to their higher density, the spherical zirconia-silicate glass grains produce a brighter SEM image than the soda-lime glass beads (Supplemental Figure 5a). These two materials can be distinguished from one another based solely on their BSE reflectance. For the shape experiment, the density of the soda-lime glass beads and angular soda-lime is the same, so BSE reflectance is not useful to differentiate the materials. Their shapes, however, are very different and can be distinguished using *iDiscover*, an image-based software. Thousands of particles in each sample were scanned and classified on the basis of their shape (Supplemental Figure 5b).

3. Analysis of Scale

Our experiments were conducted at a reduced scale relative to submarine transport systems. It is therefore important to discuss how the model turbidity currents compare to those in natural settings

on the seafloor. This comparison has three components: 1) a geometric scaling of the lobe topography; 2) a dynamic scaling of flow properties for estimating equivalence between the model and natural flows; and 3) a dynamic scaling of sediment transport in order to roughly compare particle sizes being moved by the experimental currents and those in natural settings on the seafloor. The scaling is intended to guide how experimental results are applied to the interpretation of natural turbidites. Our experiments were not designed to simulate environmental conditions associated with a specific system but rather were carried out to better understand the how composition of turbidites, the deposits of turbidity currents, vary spatially due to input compositions.

The geometric flow scaling for our experiment was done using a distorted Froude modeling scheme in which the geometric scaling ratios for vertical and horizontal dimensions are different [Graf, 1971; Cantelli et al., 2011]. We define a scale factor in the vertical direction, λ_v , as the ratio of any corresponding vertical length between prototype, or naturally occurring lobe, and model. For example, lobe thickness, λ_v is:

$$\lambda_v = \frac{H_p}{H_m} \quad (1)$$

where H_p is the thickness of a prototype lobe and H_m is the thickness of the model lobe. Next, we define the scale factor in the horizontal direction λ_H as the ratio of horizontal length between prototype and model. For example, lobe width λ_H is given by:

$$\lambda_H = \frac{L_p}{L_m} \quad (2)$$

where L_p is the width of the prototype lobe, and L_m is the width of the model lobe. As a result, the ratio between prototype and model slopes, S is:

$$\frac{S_p}{S_m} = \frac{\lambda_v}{\lambda_H} \quad (3)$$

For our experiments we use a λ_v of 100 and a λ_H of 2,500. Next, if we use an R of 1.65 (e.g. quartz) in the field and laboratory, and assume turbidity currents with constant values for flow concentration and densimetric Froude number:

$$Fr_D = \frac{\bar{u}}{\sqrt{\left(\frac{\rho_c - \rho_a}{\rho_a}\right)gh}} \quad (4)$$

at field and laboratory scale, where \bar{u} is mean flow velocity, ρ_c is current density, ρ_a is ambient fluid density, g is gravitational acceleration, and h is flow thickness, the following expressions can be derived:

$$\begin{aligned} L_p &= \lambda_H L_m; H_p = \lambda_H H_m; u_p = \lambda_V^{1/2} u_m; \\ (Q_w)_p &= \lambda_H \lambda_V^{3/2} (Q_w)_m; (Q_s)_p = \lambda_H \lambda_V^{3/2} (Q_s)_m; \quad (5a-h) \\ (t_c)_p &= \lambda_V^{1/2} (t_c)_m; C_p = C_m \end{aligned}$$

Where Q_w is flow discharge, Q_s is sediment discharge, and t_c is a characteristic time (e.g., run time).

We also calculated the flow Reynolds number:

$$\text{Re} = \frac{\bar{u}h}{\nu} \quad (6)$$

for our experimental flows, where ν is kinematic viscosity. Reynolds numbers for the model and prototype currents cannot be matched. The characteristic Reynolds number for model currents was 8000. The characteristic Reynolds number for a comparable natural current would be 6.1×10^6 . The experimental turbidity currents had a Re value that was sufficiently large to ensure the approximate Reynolds similarity for fully turbulent gravity currents proposed by *Parsons and Garcia* [1998].

Altinakar et al. [1996] document that the lower portion of velocity profiles for turbidity currents developing on a flat bed under approximately steady and uniform conditions exhibit a logarithmic form that can be described by:

$$u = \frac{u_*}{k} \ln\left(\frac{z}{z_0}\right) \quad (7)$$

where z is a distance above the bed, k is von Karman's constant and is equal to 0.407, and z_0 is a roughness parameter, equal to the elevation at which the extrapolated logarithmic velocity profile goes to zero. We have estimated the characteristic shear velocity associated with the model currents, $(u_*)_m$, by fitting (7) to velocity data collected with the PCADP from 4 current locations along the centerline of the flow. The fit to the portion of the velocity profiles situated between the bed and the velocity maximum is good. The regressions yielded $(u_*)_m$ equal to 2.9 ± 1.0 cm/s (Supplemental Figure 6). A characteristic friction coefficient, C_f , for the model currents can be calculated from the estimate for $(u_*)_m$ using:

$$u_* = \sqrt{C_f \bar{u}} \quad (8)$$

The resulting $(C_f)_m = 1.38 \times 10^{-2}$ and is consistent with other laboratory measures of $(C_f)_m$ for turbidity currents reported by *Parker et al.* [1987], *Garcia* [1994], and *Straub et al.* [2008]. A prototype shear velocity can be determined using (8) and estimated values for u_p and $(C_f)_p$. We have reduced the $(C_f)_p$ by an order of magnitude to account for the weak dependence of bed friction coefficient with turbidity current scale as summarized in *Parker et al.* [1987]. The calculated $(u_*)_m = 0.063$ m/s.

Grain sizes used in the experiment can be compared to natural systems by estimating equivalent sediment transport conditions between the experimental and natural systems. For this comparison we will focus on the spherical glass sediment utilized in both experiments, but a similar analysis could be done for the angular soda-lime glass and spherical zirconia-silicate glass grains. Since the predominant mode of transport is suspended load, we make the dynamic comparison by matching the ratio w_s/u_* . This scaling parameter was chosen because it best characterizes the degree that particles of various sizes are suspended within the transporting current, with w_s serving as the scale value for downward particle advection and u_* being the scale value for the effective diffusion of particles into the interior of the flow by turbulent eddies. Particle settling velocities for D10, D50, and D95 equaled 4.7×10^{-3} m/s, 7.6×10^{-3} m/s, and 1.5×10^{-2} m/s, respectively. Calculated experimental values for $w_s/u_{*(D5)}$, $w_s/u_{*(D50)}$, and $w_s/u_{*(D95)}$, are 1.6×10^{-1} , 2.6×10^{-1} , and 5.2×10^{-1} , respectively. All of these values are $\ll 1$, the minimum value for significant suspension transport originally reported by *Bagnold* [1966]. By satisfying the equality $(w_s/u_*)_m = (w_s/u_*)_p$ we estimated D5, D50, and D95 for the spherical glass sediment in the experimental flows correspond to particle sizes of 131 μm , 182 μm , and 289 μm , respectively at field scale.

The sediment-transport scaling derived above is used to estimate properties associated with the interiors of currents. Near-bed conditions are calculated using the particle Reynolds number:

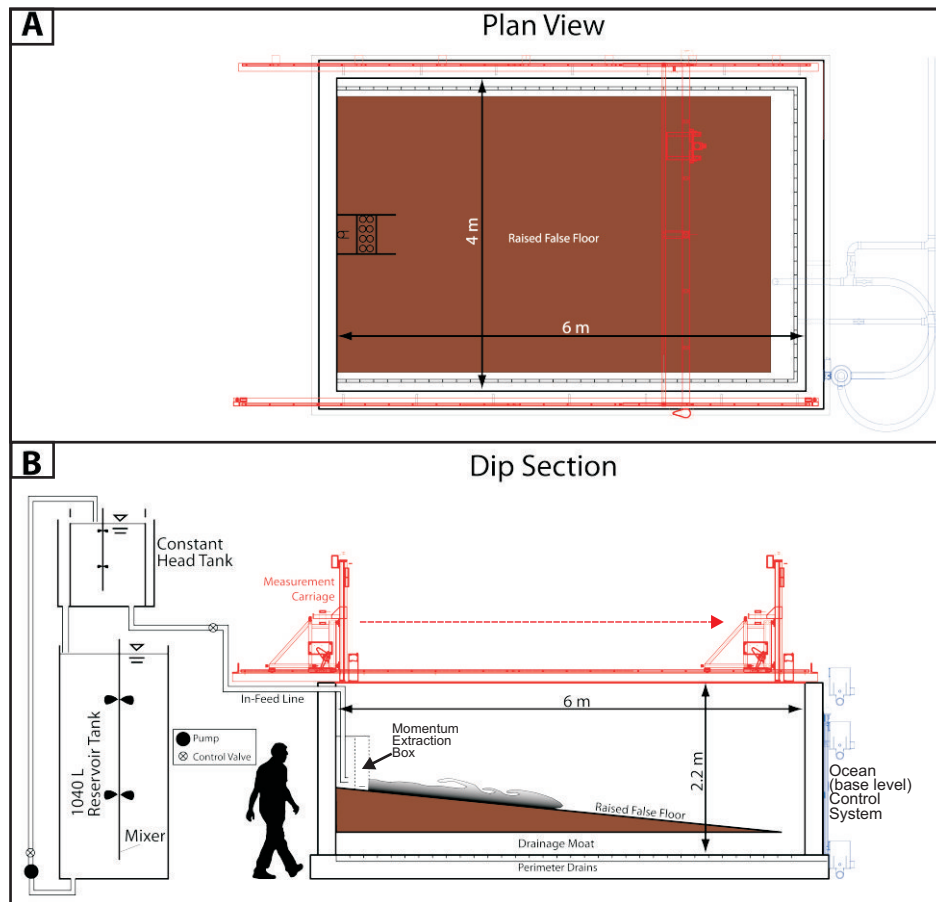
$$\text{Re}_p = \frac{u_* D}{\nu} \quad (9).$$

The appropriate model and prototype values for u_* and D95, as well as $\nu = 1.0 \times 10^{-6}$ m²/s yield estimates for $(\text{Re}_p)_m$ and $(\text{Re}_p)_p$ of 4.8 and 18.3, respectively. For the case of a flat bed the experimental system has a hydraulically smooth boundary and the natural system has a hydraulically transitional boundary, implying that scale of particles composing the beds is smaller than (model) or comparable to (prototype) the thickness of the viscous sublayer [*Graf*, 1971]. In both cases viscous effects are important in setting the style of the near-bed sediment-transport conditions. *Nino et al.* [2003] performed a set of experiments to determine threshold conditions for

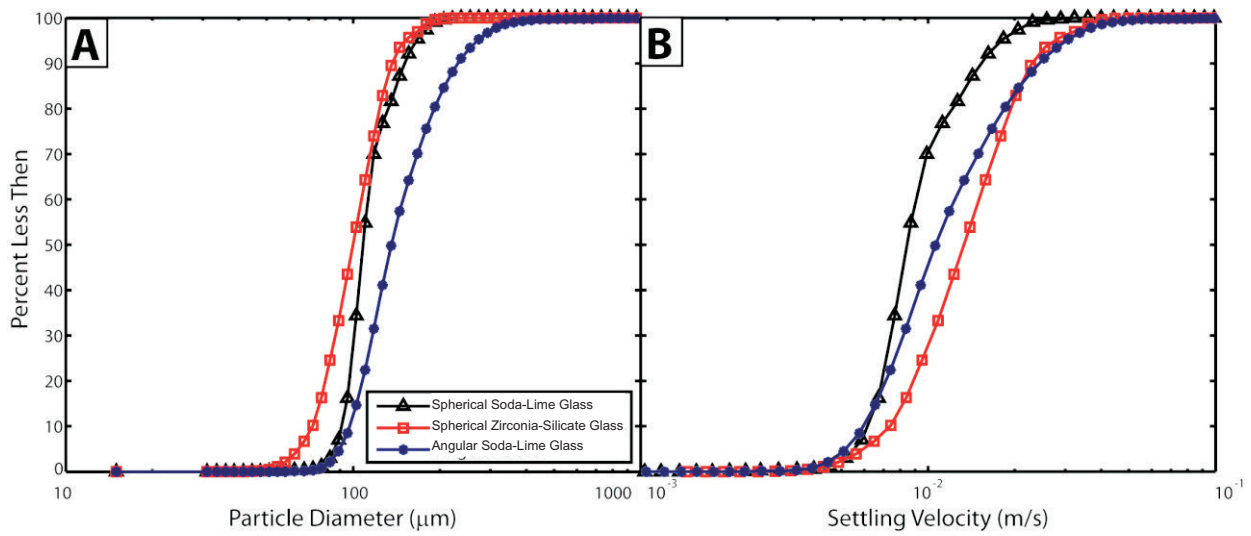
the entrainment of bed sediment into suspension for cases of small Re_p where viscous effects are significant. These threshold conditions for particle entrainment into suspension are plotted in Supplemental Figure 7 as functions of Re_p , u^*/w_s , and dimensionless bed shear stress ($\tau^*=u_*^2/[RgD]$). Estimated values for Re_p , u^*/w_s , and τ^* for our experiment are also plotted in Supplemental Figure 7. These values indicate that experimental conditions associated with our model lie within the suspension regime as measured and predicted by *Nino et al.* [2003]. A full comparison of model and prototype geometry, flow, and sediment transport properties is given in Supplemental Table 1.

References

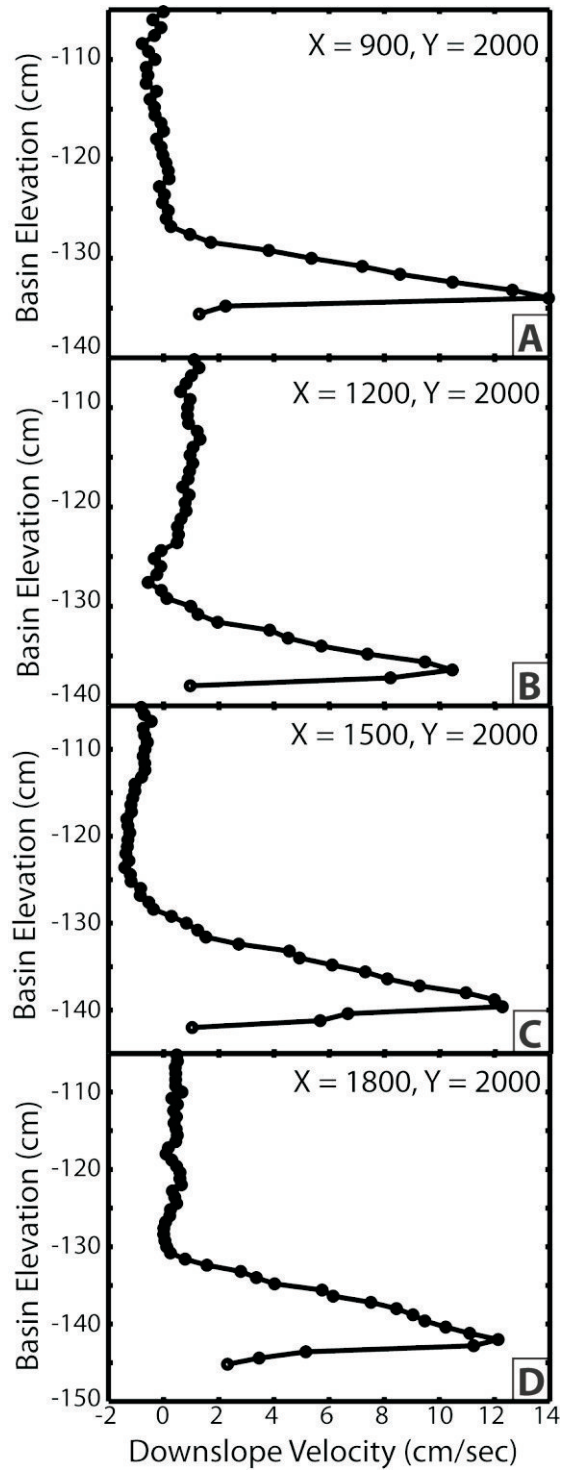
- Altinakar, M.S., W.H. Graf, and E.J. Hopfinger, 1996, Flow structure in turbidity currents: *Journal of Hydraulic Research*, v. 34, p. 713-718.
- Bagnold, R.A., 1966, An approach to the sediment transport problem from general physics, U.S. Geological Survey Professional Paper, 37 p.
- Cantelli, A., C. Pirmez, S. Johnson, and G. Parker, 2011, Morphodynamic and Stratigraphic Evolution of Self-Channelized Subaqueous Fans Emplaced by Turbidity Currents: *Journal of Sedimentary Research*, v. 81, p. 233-247.
- Ferguson, R.I., and M. Church, 2004, A simple universal equation for grain settling velocity: *Journal of Sedimentary Research*, v. 74, p. 933-937.
- Garcia, M.H., 1994, Depositional turbidity currents laden with poorly sorted sediment: *Journal of Hydraulic Engineering*, v. 120, p. 1240-1263.
- Graf, W.H., 1971, *Hydraulics of sediment transport*: New York, McGraw-Hill, 513 p.
- Nino, Y., F. Lopez, and M.H. Garcia, 2003, Threshold for particle entrainment into suspension: *Sedimentology*, v. 50, p. 247-263.
- Parker, G., M.H. Garcia, Y. Fukushima, and W. Yu, 1987, Experiments on turbidity currents over an erodible bed: *Journal of Hydraulic Research*, v. 25, p. 123-147.
- Parsons, J.D., and M. H. Garcia, 1998, Similarity of gravity current fronts: *Physics of Fluids*, v. 10, p. 3209-3213.
- Straub, K.M., D. Mohrig, B. McElroy, J. Buttles, and C. Pirmez, 2008, Interactions between turbidity currents and topography in aggrading sinuous submarine channels: A laboratory study: *Geological Society of America Bulletin*, v. 120, p. 368-385.
- Turner, J.S., 1973, *Buoyancy effects in fluids*: Cambridge, U.K., Cambridge University Press, 292 p.



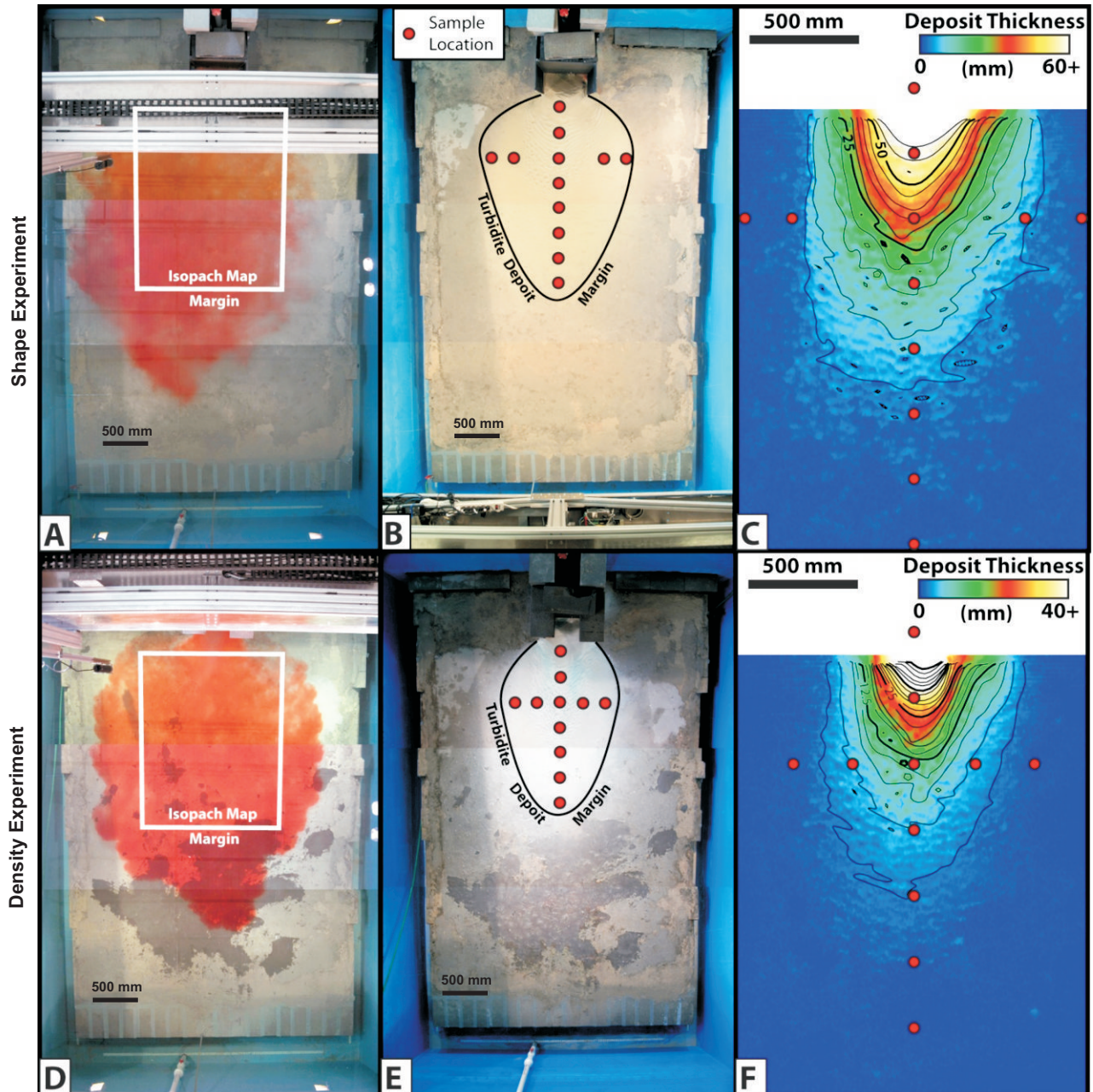
Supplemental Figure 1. Schematic diagram of the experimental facility. (A) Plan view of the basin. Each current passed through a momentum extraction box located against the middle of the left wall of the basin prior to entering the basin. Once in the basin, currents were free to expand laterally and flow down the false floor (brown region). Surrounding the false floor was a moat used for collection of currents following its passage over the false floor, reducing reflections off of tank walls. (B) Side view of the facility. Each current is mixed in a reservoir tank and pumped into a constant head tank before entering the basin.



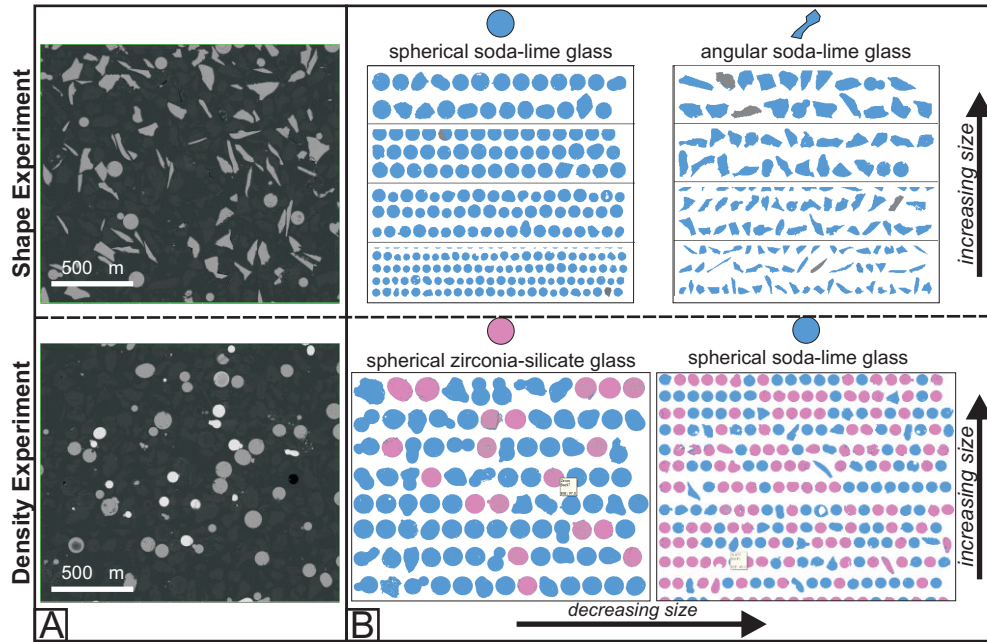
Supplemental Figure 2. Particle size (A) and particle settling velocity (B) distributions for the three sediment types used in this study.



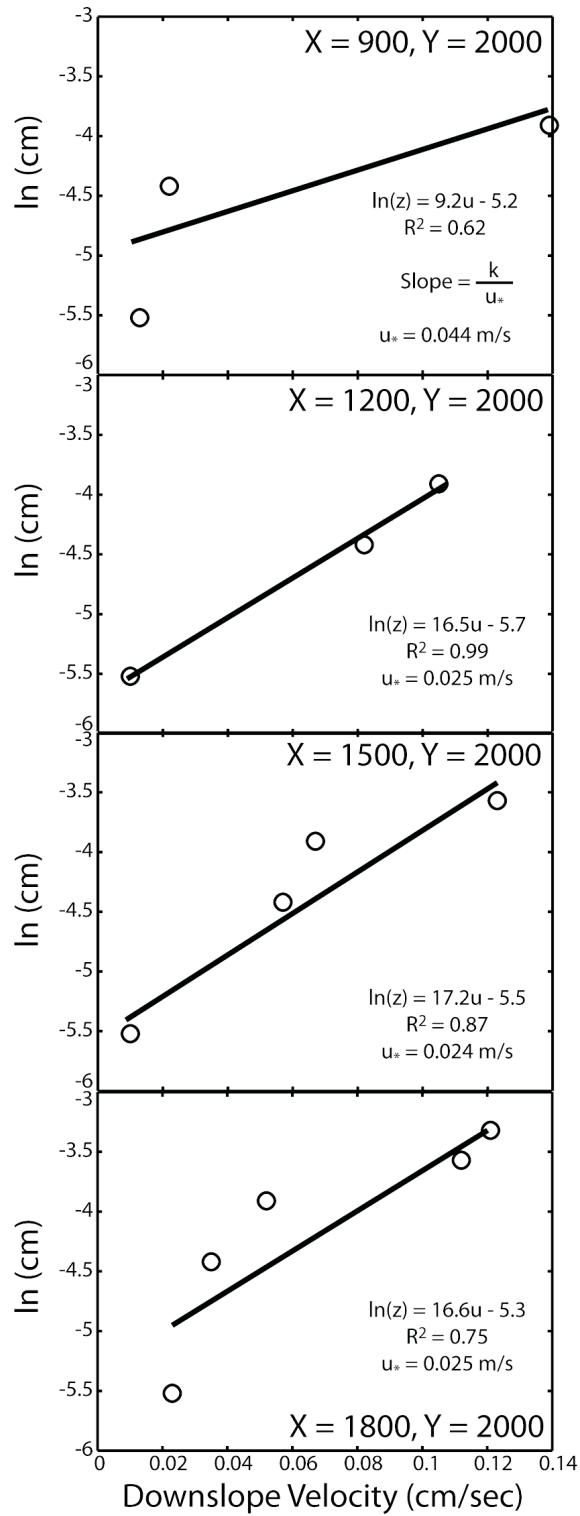
Supplemental Figure 3. Profiles of downstream velocity for currents measured at the basin centerline, with increasing downslope distance using PCADP.



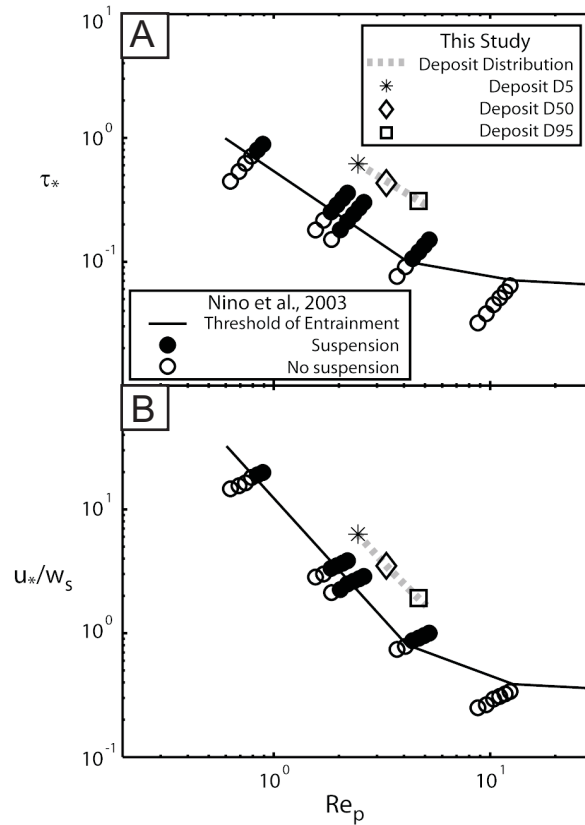
Supplemental Figure 4. Photographs of experimental flows, deposits, and topographic maps of experimental deposits. (A) Photograph of 1st flow event of the shape experiment in basin. Basin entrance box is located in center top of image. Red dye injected into current at basin entrance to aid visualization. (B) Image of experimental deposit resulting from shape experiment. Red circles mark locations where deposit samples were collected for characterization of deposit particles. (C) Map of deposit thickness from sedimentation by five turbidity currents in the shape experiment. This map is the difference of a map of the basin collected prior to the first experimental current and a map collected after the fifth experimental current. Contour interval is 5 mm. Location of map relative to basin is shown in (A). (D) Photograph of 1st flow event of density experiment in basin. Basin entrance box is located in center top of image. Red dye injected into current at basin entrance to aid visualization. (E) Image of experimental deposit resulting from density experiment. Red circles mark locations where deposit samples were collected for characterization of deposit particles. (F) Map of deposit thickness from sedimentation by five turbidity currents in the density experiment. This map is the difference of a map of the basin collected prior to the first experimental current and a map collected after the fourth experimental current. Contour interval is 2.5 mm. Location of map relative to basin is shown in (A). Note: dark areas on the floor of the tank in the density experiment are discolorations in the mortar used on the false floor.



Supplemental Figure 5. A) SEM backscatter images from the density and shape experiments. Zirconia-silicate glass has higher backscatter reflectance than soda-lime glass and therefore the particle types in the density experiment can be easily differentiated. B) QEMSCAN images from the density and shape experiments. The QEMSCAN system can identify and classify the particles by size and shape therefore spherical soda-lime glass can be differentiated from angular soda-lime glass.



Supplemental Figure 6: Estimation of u^* for model obtained with best-fit slope of $\ln z$ vs. current velocity plots. Velocity measurements were obtained below the velocity maximum of each sample profile. Mean u^* value of the five flow locations presented equaled 2.9 ± 1.0 cm/s.



Supplemental Figure 7. Comparison of experimental conditions in this study to threshold of particle entrainment into suspension conditions reported by Nino et al.. Circles represent measurements of Nino et al. and black solid lines are proposed threshold conditions. Gray dashed line represents experimental conditions in this study defined between D5 and D95 particle sizes of input sediment distribution. A) Threshold of particle entrainment into suspension defined by Re_p and t_* . B) Threshold of particle entrainment into suspension defined by Re_p and u^*/w_s .